Article

Laser Patterned Alumina Mask and Mask-less Dry Etch of Si for Light Trapping

Jovan Maksimovic[1,†], Haoran Mu[1,†], Daniel Smith[1], Tomas Katkus[1], Mantas Vaičiulis[2], Ramūnas Aleksiejūnas[2], Gediminas Seniutinas[3], Soon Hock Ng[1,4,*] and Saulius Juodkazis[1,5,*]

1 Optical Sciences Centre and Australian Research Council (ARC) Industrial Transformation Training Centre in Surface Engineering for Advanced Materials (SEAM), Swinburne University of Technology, Hawthorn, VIC 3122, Australia
2 Institute of Photonics and Nanotechnology, Vilnius University, Saulėtekio Ave. 3, 10257 Vilnius, Lithuania
3 Optical Sciences Centre, School of Science, Swinburne University of Technology, Hawthorn, Vic 3122, Australia
4 Melbourne Centre for Nanofabrication, 151 Wellington Road, Clayton Vic 3168, Australia
5 WRH Program International Research Frontiers Initiative (IRFI) Tokyo Institute of Technology, Nagatsuta-cho, Midori-ku, Yokohama, Kanagawa 226-8503 Japan
* soonhockng@swin.edu.au (S.H.N); saulius.juodkazis@gmail.com (S.J.)
† These authors contributed equally to this work.

Abstract: Ultra-short 230 fs laser pulses of 515 nm wavelength were tightly focused into 700 nm focal spots and utilised in opening $\sim 0.4-1$ μm holes in alumina Al_2O_3 etch masks with 20-50 nm thickness. Such dielectric masks simplify fabrication of photonic crystal (PhC) light trapping patterns for the above-Lambertian performance of high efficiency solar cells. Conditions of laser ablation of transparent etch masks and effects sub-surface Si modifications were revealed by plasma etching, numerical modeling, and minority carrier lifetime measurements. Mask-less patterning of Si is proposed using fs-laser direct writing for dry plasma etch of Si.

Keywords: light trapping; Si solar cells; ablation; dry etch; Lambertian limit

1. Introduction

Solar cells are the ultimate large area application where solar-to-electrical efficiency improvements can bring significant increases for sustainability and energy efficiency targets [1–5]. Cell efficiency is considered the critical parameter driving commercial development for industrial applications and consequently is the focus of most research; specifically, approaching the theoretical Shockley-Queisser (SQ) light-to-electrical conversion efficiency limit of 33.5% for Si [6]. Life-Cycle-Assessment (LCA) assesses the environmental impact of energy generation solutions based on greenhouse gas emissions created over the life-cycle of the energy source. Monocrystalline Si-based solar cells are made from a highly abundant material but require significant energy for purification and crystallisation; as such, it has one of the highest environmental impacts of all the solar technologies, 29.0-671.0 g CO_{2eq}/kWh [7]. This, however, is still much lower than coal (750–1050 g CO_{2eq}/kWh), and with Si being the most mature solar technology, any increase in efficiency contributes to reducing environmental impact. This is particularly important for the current state of climate change which is defined as "code red for humanity" in the last Intergovernmental Panel on Climate Change (IPCC) Working Group 1 report on the physical science basis (Aug. 2021). The need to reduce emissions and wean humanity off fossil fuels requires investments into every facet of renewable energy generation.

Before new solar cell designs becomes ready for industrial upscaling, improvements of technology have to be independently tested on the centimetre scale at certified labs. Hence, a fs-laser direct write of an etch mask in a Cr film of tens-of-nanometres thickness was demonstrated for large area, 2×2 cm^2, Si solar cell surface texturing for photonic crystal

 doi:10.20944/preprints202212.0583.v1

(PhC) patterns [8]. Dry or wet etching of inverse pyramidal (or tee-pee) patterns were carried out through sub-1 μm openings in the mask. It was theoretically demonstrated [9–15] and experimentally validated [16] that a PhC light trapping is required to break Lambertian (ray optics) light trapping for solar-to-electrical power conversion efficiencies above current record efficiencies around 27% and approaching the single junction limit for Si at $\sim$ 32% (one Sun) [17]. The world record equalling efficiency of $\sim$ 25% has been demonstrated (Panasonic R&D) using a simple low temperature passivation via hydrogenation of amorphous Si (a-Si:H) in heterojunction. In Sept. 2016, Kaneka Ltd. reported a new record of 26.33% [18], with a Interdigitated Back Contact (IBC) design delivering record high performance with surface of random-pyramids for light trapping using a 300-μm-thick Si solar cells.

Light trapping PhC pattern convert incoming sun light, which is normal to the surface, into in-plane modes and promotes absorption even in micro-thin Si (or any other light absorbing material/composite). Figure 1(a) illustrates light field enhancement inside a $\sim$ 1.3 μm thick Si solar cell with light trapping inverse-pyramidal pattern with period of $\Lambda = 1.3$ μm at the wavelength $\sim$ 1 μm close to the absorption edge. The wave nature of light via interference of the slab modes is harnessed for increased absorption. Absorption and scattering cross sections $\sigma_{ab.sc}$ are shown in Fig. 1(b,c), respectively. The difference in absorption of a $5-\mu$m-thick unpatterned slab of Si and textured by PhC is highlighted in (b) and can reach more than 50%. Over the range of 5-to-15 μm thickness there is distinct and constant increase of absorption with Si thickness at the longer wavelengths close to the bandgap edge $\sim$ 1 μm. This increase in absorption is aligned with reduced scattering (reflection is accounted in σ_{sc}). This qualitative illustration of PhC light trapping in Si has been demonstrated experimentally in PhC surface patterns fabricated using electron beam lithography (EBL) defined etch masks with rectangular openings in SiN-mask [16]. Utilising a Si-on-insulator (SOI) with $\sim$10 μm-thick Si device layer samples, Lambertian limit was surpassed at the longer wavelength range where improvement of light trapping can bring the most of increase in solar cell efficiency; it was demonstrated over 1×1 cm^2 area patterns. This demonstration of superior optical light absorption invites a next challenge to apply it to real solar Si cells and fabrication over larger areas, since robust SiN-masks which can withstand etching requires high temperature growth above 250°C using chemical vapour deposition (CVD).

One of the most promising geometry of high-efficiency Si solar cells is IBC cells where surface patterning by PhC is most easy to incorporate into fabrication sequence [19,20]. After steps of doping and integration of contacts, sealing of the back-side with cross-linked SU8 resist that can withstand a sequence of wet and plasma etch steps, including piranha and HF solution treatments if required, has to be developed next. EBL or direct laser writing of etch masks can be used where the latter is more practical, since it does not require vacuum and can be applied over large surface areas. Plasma etching using laser ablated circular micro-holes is faster than KOH wet etching by an order of magnitude. Plasma etch is another necessary development for thinning of Si IBC cells to the thickness range where light trapping by PhC patters is the most promising, i.e., 10-30 μm from typical 190-290 μm Si cells currently developed. At achievable plasma etching rate of Si at $\sim (1-2)$ μm/min, practically achievable 1-2 hour process time will be required. Most importantly, the surface height distribution over the etched areas is of paramount importance. In this respect, direct laser writing of etch mask is less sensitive to micrometre-scale unevenness of surface height as compared to the more demanding EBL approach. Investigations were carried out in this study to address some of next challenges in laser mask writing over large areas and developing masks which are not based on metals (e.g., Cr).

Preprints (www.preprints.org) | NOT PEER-REVIEWED | Posted: 30 December 2022 doi:10.20944/preprints202212.0583.v1

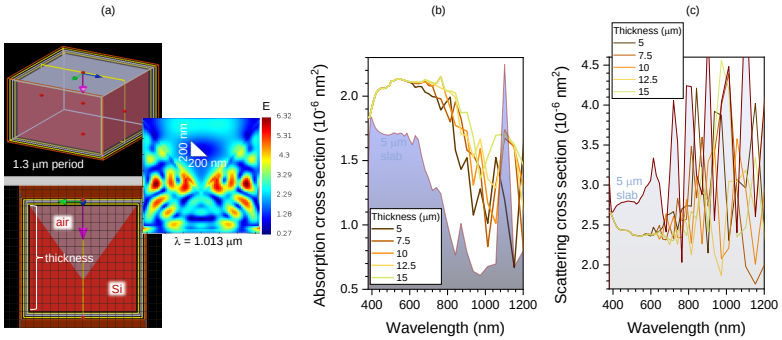

Figure 1. Numerical modeling of light trapping by photonic crystal (PhC) on Si. (a) Numerical model and a central cross section of light enhancement in 1.3 μm thick Si; period of PhC $\Lambda = 1.3$ μm. Calculated by finite difference time domain (FDTD; Lumerical, Ansys). (b) Absorption cross section σ_{ab} of Si of different thicknesses for PhC $\Lambda = 1.3$ μm. Background spectral profile is for a flat slab of Si of 5 μm. (c) Corresponding scattering cross sections σ_{sc}. The indirect Si bandgap at 300K is 1.12 eV or 1.107 μm wavelength.

Here, different conditions of laser mask definition by ablation was tested for different thickness of alumina (Al_2O_3) masks and plasma etch conditions over areas with centimeters in cross section. Dielectric etch masks using alumina films compatible with anti-reflection coatings of IBC cells as well as mask-less etching of Si were tested experimentally and by numerical modeling. Changes of minority carrier lifetime was monitored during processing steps using photo-conductivity method used in industrial Si solar cell production. A mask-less laser patterning with plasma etching of Si was tested.

2. Samples and Methods

Silicon wafers of $\langle 001 \rangle$ surface orientation were coated with Al_2O_3 by electron-beam evaporation (Axxis, JKLesker). Femtosecond (fs-)laser irradiation was implemented for ablation of holes in the mask for subsequent dry plasma etching of Si.

Femtosecond (fs-)laser microfabrication setup based on Pharos (Light Conversion) fs-laser was integrated with scanning Aerotech xy-stages and SCA software control of laser radiation and scanning conditions (Workshop of Photonics). Pulse-to-pulse energy stability of laser was $\sim 1\%$ as monitored directly over long ~ 1 h time. This was important due to sensitivity of ablated hole diameter in the mask over long laser writing time. Si samples were placed on a 10×10 cm^2 porous ceramic chucking plate with a steel retainer with a flatness of 10 μm. This determined a well defined sample plane, provided there were no micro-particulates between the sample and vacuum chuck, which can cause bending of thin samples.

The plane approximating sample's surface was calculated using three points $P_{1,2,3}$ method [21] where the coordinates of the focal point placed on the sample's surface are determined. The plane through the point P_1 (also P_2 and P_3) is given by $a_n(x - x_1) + b_n(y - y_1) + c_n(z - z_1) = 0$ with the normal coefficients (a_n, b_n, c_n) determined experimentally. This is the plane equation which will account for the actual tilt, if any. During laser writing, for the each new irradiation point $P_{new}(x_{new}, y_{new})$ along the writing trajectory, the height z_{new} is calculated from the plane equation given above. This accounted for the actual surface position. During writing over larger surface areas for long time, the three-points method can be re-applied accorss smaller areas to keep the surface within the depth of focus.

Dry plasma etching was carried out using reactive ion etching (RIE) tool (Samco) using established recipe for PhC patterns: SF_6:CHF_3:O_2 at 5:1:1 flow rate ratio for 10-15 min. Inductively coupled plasma (ICP) power was 180 W with 0 W RF (radio frequency) bias power for the Cr mask and 140 W and 5 W for the alumina mask.

 doi:10.20944/preprints202212.0583.v1

Scanning electron microscopy (SEM) was used for structural characterisation of samples processed by laser and plasma treatments (Raith 150TWO electron beam writer was used in a field-emission SEM mode).

Minority carrier lifetime was measured by the inductively coupled photo-conductance method with Sinton 3000 (WCT-120), which is an established tool in the Si solar cell industry. Changes of current J_{ph} due to photo-induced carriers over time t after a Si sample/wafer was illuminated by a flash lamp is measured inductively and is read out as a voltage V_{in} across a reference resistance. The measured voltage transient $J_{ph}(t) = fV_{in}(t)[\text{Const}_i \times 38\ \text{mA/cm}^2]$, where f is the optical factor dependant on the optical properties of the wafer (surface texture, thickness, anti-reflection coating), Const_i is the constant determined by Sinton Instruments for individual testers and the value of 38 mA/cm^2 is the approximate short-circuit current density J_{SC} of the reference cell under standard test conditions (the air mass AM 1.5 solar spectrum). Typical values of $f = 0.67 - 0.73$ are for a planar wafer with no anti-reflection coating, (0.80 - 0.95) for a planar wafer with an anti-reflection coating and (0.95 - 1.15) for a textured wafer with an anti-reflection coating. For samples with PhC texture, $f = 0.95$ was used for all samples measured. An instantaneous lifetime determined from the measured J_{ph} current transient is the minority carrier lifetime τ_{mc}. It was used to trace changes of surface quality due to recombination during different processing steps.

Approximately 300 μm thick and micro-thin (12-μm-thick) n- and p-type Si wafers were used in this study. A handling protocol was developed for thin-Si wafer for cutting and patterning. A 4-inch Si (fixed on a plastic film on a ring-mount) was placed onto a transparent 4-inch Al_2O_3 crystalline wafer ($\sim$ 300 μm thickness) using $\sim$ 10 μm coatings of SU8 or AZ photoresists as a glue. After separation from the film, Si was cut into smaller pieces of arbitrarily sizes as required for experiments by fs-laser dicing (irradiation from the Si side). Release of Si cut-out chips was made by placing entire Si-Al_2O_3 sandwich into a developer. Organic developer was diluted by IPA rinse and the floated Si-chips were transferred from rinse solution onto a desired substrate (e.g., cover or slide glass) for further fabrication and characterisation procedures.

3. Results and discussion

3.1. Laser ablation of transparent mask

Numerical modeling of light intensity at the focal region was modeled using finite difference time domain (FDTD; Lumerical, Ansys). Figure 2 shows light intensity distribution in the plane of incidence for focusing of $\lambda = 515$ nm wavelength into 700 nm focal spot placed at the surface of the mask (0.65 μm from light source while Si surface is at 0.7 μm distance). This closely corresponds to the experimental conditions of mask ablation using an objective lense with numerical aperture $NA = 0.9$, i.e., diameter at focus $2r = 1.22\lambda/NA = 698$ nm. Light distribution through the mask reveals that slightly less intensity is reflected and more is irradiated inside Si for a thicker 50 nm alumina mask (see horizontal dashed-line in Fig. 2). This is an effect of partial anti-reflection coating due to refractive index of alumina $n = 1.7$ (used in FDTD). The anti-reflection coating for a single wavelength has to be $\lambda/4 = 129$ nm thickness for 515 nm and the refractive index $n_{arc} = \sqrt{n_{Si}} = 1.87$. Figure 2 shows only minor variation of E-field intensity throughout the thickness of the mask ($|E|$ amplitude is plotted while the intensity is E^2); for comparison a non-transparent 30 nm Cr mask is also shown. Apparently, ablation of transparent films is affected by their anti-reflection action similarly as for the membranes [22].

Preprints (www.preprints.org) | NOT PEER-REVIEWED | Posted: 30 December 2022 doi:10.20944/preprints202212.0583.v1

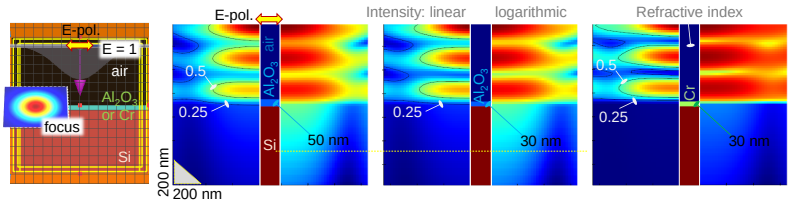

Figure 2. Numerical modeling of light focused onto 700 nm diameter on the sample surface for $\lambda = 515$ nm wavelength. Linear E and $\lg E$ distributions are shown; the incident light E-field is $E = 1$. Contours for $E = 0.5$ and $E = 0.25$ are shown. Central cross section shows refractive index distribution across the light propagation. Left panel shows the calculation volume in finite difference time domain (FDTD) model (Lumerical, Ansys).

Despite laser ablation taking place at high pulse intensity > 1 TW/cm^2 via nonlinear light matter interaction, the linear optical properties such as antireflection coatings play an important role. This increased energy per pulse required to open an ablation hole in the alumina mask when it became thicker. In the case of 20 nm as well as 50 nm masks, Si ablation caused hole opening in a transparent mask and brittle failure of Al_2O_3 was observed at near threshold fluence rather than melting, as it was for the Cr mask.

Next, we explored the power dependence of the hole ablation in a 50-nm-thick Al_2O_3 mask on a 12-μm-thick Si wafer via the standard $Diameter^2$ power dependence (Figure 3; see Supplement). Slightly different thresholds for $\lambda = 515$ nm and 1030 nm were observed and fluence $F_p = 0.25$ J/cm^2 and 0.47 J/cm^2, respectively. This is close to the Si ablation threshold at 0.2 J/cm^2 for 515 nm, which is absorbed. The first harmonic 1030 nm laser pulses are in the spectral window of Si. At close to the threshold fluences, in both cases of λ, there was evidence of brittle failure of the Al_2O_3 mask (see SEM images in Figure 3(b)). Ablation of Al_2O_3 coated Si was carried out in such a way that there was no back reflected laser pulse for the 1030 nm case where sample is transparent. Shorter 515 nm wavelength is better suited for mask ablation due to a lower slope of D^2 vs. E_p dependence, which affords some leeway to make the same ablation hole size in the mask, regardless small laser power fluctuations. Also, there is no ns-pedestal emission from laser due to long excitation pulse from laser diodes used as a pump source in a solid-state laser. This fs-laser ablation surface texturing (FAST) was used to make etch mask on Si.

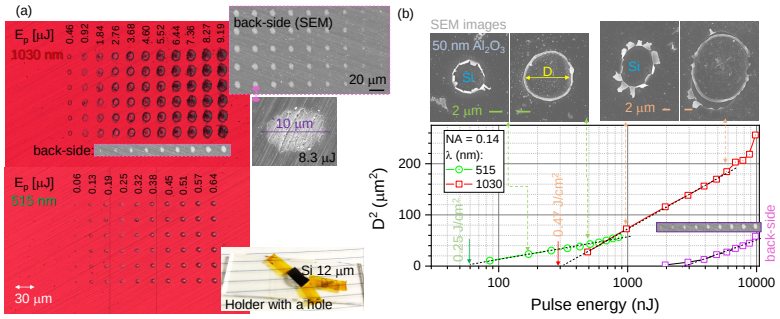

Figure 3. (a) Optical reflection image of single-pulse irradiated sites at $NA = 0.14$ focusing on a 50-nm Al_2O_3 coated 12-μm-thick Si (inset photo) at different pulse energies E_p (on the sample) and wavelengths $\lambda = 1030$ nm and 515 nm. SEM image insets show the back-side damage of the 12-mum-thick Si. (b) Ablation threshold of 50-nm-thick Al_2O_3 film on 12-μm-thick Si determined from $D^2 \propto \lg(E_p)$ dependence for two wavelengths $\lambda = 1030, 515$ nm at $NA = 0.14$ focusing; E_p was measured on the sample. The diamater of the back-side contrast change in SEM image is plotted on the same D^2-dependence (for $\lambda = 1030$ nm).

Interestingly, there were well recognisable surface modification marks on the opposite side of the sample for the $\lambda = 1030$ nm ablation (see SEM inset in Figure 3(a)). The diameter of the laser-modified region was ~3 times smaller than on the front surface (b). The difference of slope (smaller) in the power dependence $D^2 \propto E_p$ signifies a different nonlinear dissipation of pulse energy over propagation through the 12-μm-thick Si (see

Preprints (www.preprints.org) | NOT PEER-REVIEWED | Posted: 30 December 2022 doi:10.20944/preprints202212.0583.v1

Sec. 3.4). The exit plane had apparent ablation of nanoscale grooves on Si back-surface, which were present on the Si surface (see SEM inset in Figure 3(a)). The entire 12 μm thickness of Si is inside the depth-of-focus or double Rayleigh length $2z_r = \pi r^2/\lambda \approx 62$ μm.

Figure 4 illustrates an experimental finding that 20-nm-thick alumina did not withstand the required 10-15 min plasma etch of Si and failed mechanically. If the pattern on the mask is made in steps of 1 mm in one direction over the entire 1×1 cm^2 area, the mask was mechanically robust enough to survive plasma etch. No mechanical failure was observed when mask was 50 nm thick even for the entire 1×1 cm^2 area.

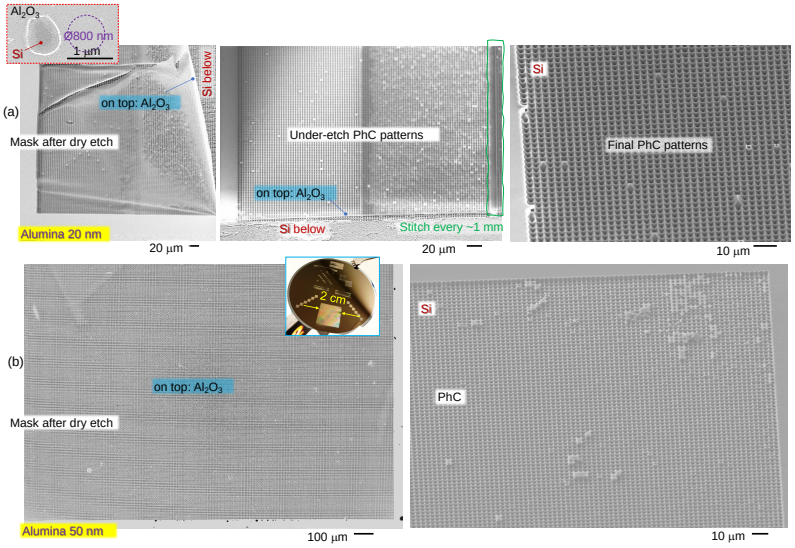

Figure 4. (a) SEM images of Al_2O_3 mask (20 nm) after plasma etch and the final PhC pattern on Si. Middle panel shows implemented strategy to introduce few-μm-wide bridges every 1 mm to prevent mask failure (left panel) due to under-etch. Pulse energy to open ablation hole was $E_p = 12.5$ nJ (on sample). Inset shows ablation opening in the mask which match exactly the focal diameter of 0.8 μm (before etch) close to focal diameter $1.22\lambda/NA = 700$ nm. (b) Mask of 50 nm of Al_2O_3 (left image) was maintaining mechanical strength for plasma etch over 1×1 cm^2 areas. Si patterned using 50 nm alumina mask after ultra-sonic mask removal (right image). Etched by SF_6:CHF_3:O_2 at 5:1:1 flow rate ratio for 10 min. Pulse energy to open ablation hole was $E_p \approx 12$ nJ (on sample). Inset shows photo of wafer scale patterning tests used for optimisation of larger area laser writing.

3.2. Deep-etch of Si

Deeper structures were obtained by applying small bias power of 5 W and decresing the ICP power to 140 W. The ICP power is responsible for isotropic (all directional) etch while direct bias enhances directionality of etching normal to the surface. The total ICP and bias powers are usually kept close to constant, i.e., if ICP is reduced the bias can be increased. This was tested for the deeper etch (Figure 5). Plasma etching and ion sputtering has inherently strong dependence on angle of incidence onto the surface. The fastest material removal is at 70-80° angles. This directional etch favors formation of deeper holes with close to vertical walls as observed experimentally. It is well established that isotropic Ar-plasma etch has very fast removal of fs-laser modified regions [23]. This can be one of the reasons why deeper plasma etched tee-pee patterns were fabricated. The Si etch used is slightly anisotropic, especially when used in the under-etch mode through small openings in the mask. This is judged from tee-pee profiles which still have resemblance to inverse pyramid patterns obtained in an anisotropic KOH wet etch. The typical aspect ratio of the $depth/width \approx 1$ for the wet and dry etch using 30 nm Cr and 20 nm alumina masks is increased to ≈ 2. Thinning of 50 nm alumina mask by etching was also recognisable by color change (see color photo in Figure 5 and Supplement A) in the non-patterned regions. Such thinning could contribute to the mechanical failure of thinner 20-nm-masks under prolonged etching.

Preprints (www.preprints.org) | NOT PEER-REVIEWED | Posted: 30 December 2022 doi:10.20944/preprints202212.0583.v1

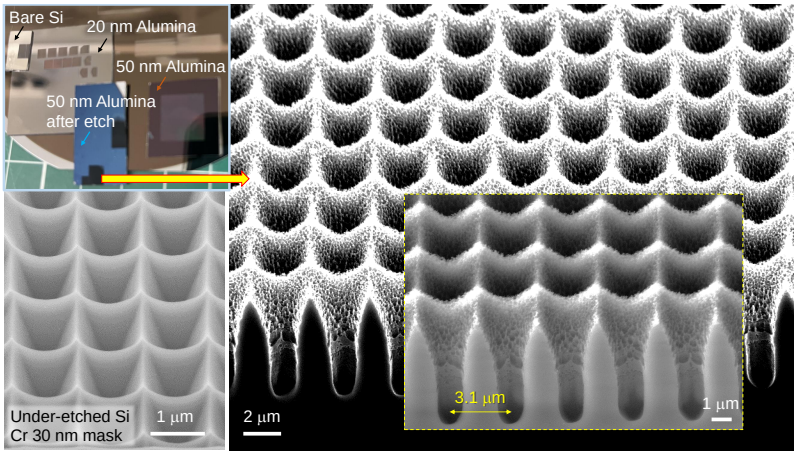

Figure 5. Color-photo shows Si samples with different Al_2O_3 masks before and after dry plasma etch. Left-SEM image show Si PhC made by plasma etch developed for an under-etch zero-ridge tee-pees PhC pattern using 30-nm-thick Cr mask [8]. Similar plasma etching conditions as used in the case of 30 nm of Cr showed very different tee-pees pattern for the 50 nm alumina mask ablated by $E_p \approx 4.2$ nJ pulses (at focus). Etched by SF_6:CHF_3:O_2 at 5:1:1 flow rate ratio for 15 min at ICP 180 W and 0 W bias (Cr-mask) [8] and 30 min at ICP 140 W and 5 W bias (Al_2O_3-mask); He pressure 2.70 kPa at a process pressure of 2.5 Pa.

3.3. Mask-less etch of Si

Figure 6 compares two different PhC fabrication methods on Si surface. When direct laser ablation by FAST was used without any mask to make ablation pattern of the required periodicity on the surface, only $E_p = (1-2)$ nJ was required. When Si was ablated to open holes in a 20-nm-thick Al_2O_3 mask, an order of magnitude larger pulse energy > 10 nJ was necessary. This is caused by reflection change due to the coating (Fig. 2) as well as ablation pressure required to break through the alumina nano-film. The average intensity for $E_p =$ 2 nJ (on sample) was $I_p = F_p/t_p = 2.27$ TW/cm^2 for fluence $F_p = E_p/(\pi r^2) = 0.52$ J/cm^2, where radius of the focal spot $r = 0.61\lambda/NA = 349$ nm for $NA = 0.9$, $\lambda = 515$ nm and pulse duration $t_p = 230$ fs. This corresponds to approximately double the ablation threshold of Si for ultra-short sub-1 ps pulses which is ~0.2 J/cm^2. [24]

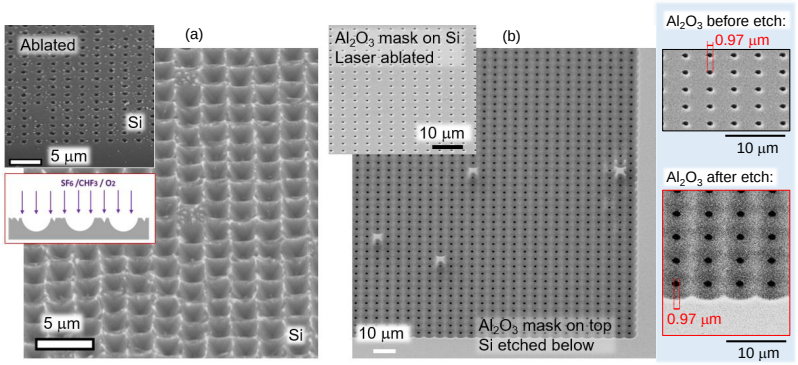

Figure 6. (a) Maskless pattering of Si with PhC light trapping structures using fs-laser ablation and dry plasma etch. Pulse energy $E_p \approx 3.2$ nJ (at focus), $NA = 0.9$. Inset shows just ablated surface of Si. (b) Si pattering by plasma etch using 20-nm-thick Al_2O_3 mask. $E_p = 4.2$ nJ (at focus), $NA = 0.9$. Left-insets show closeup views of laser ablated openings in the mask which have diameter ~ 1 μm for the 20-nm-thick Al_2O_3. Dry plasma etch conditions were same as for Al_2O_3-mask with the bias set at 5 W (a directional etch promoted).

The ablation threshold fluence F_{th} [J/cm^2] of Si and Gaussian beam waist w_0 were experimentally established from the single pulse ablation dependence of the diameter of the ablated crater D_a vs. pulse energy ln E_p: $D_a^2 = 2w_0^2 \ln E_p$.

Preprints (www.preprints.org) | NOT PEER-REVIEWED | Posted: 30 December 2022 doi:10.20944/preprints202212.0583.v1

3.4. Energy deposition and nonlinear light-matter interaction (above ablation threshold)

In order to test the conjecture of structural modification of Si along the propagation of a fs-laser pulse during mask writing, a separate experiment was carried out using single crystal 10-μm-thick Si wafer (orientation $\langle 001 \rangle$). By measuring transmitted pulse energy vs. the incident, a nonlinear light-matter interactions can be determined from a departure from the linear dependence. Measurements were carried out at lower $NA = 0.14$ with change of position on the sample for each incident pulse energy. When two-photon absorption (TPA) dominates (non linear absorption), the transmitted intensity through the sample of thickness d is $I_t(d) = \ln(1 + I_{in} d\beta)/(d\beta) + Const$, where β [cm/W] is the TPA coefficient (the nonlinear intensity dependent absorption coefficient $\alpha(I_{in}) = \alpha_0 + \beta I_{in}$). This dependence is only valid when other nonlinear absorption mechanisms are absent, which is usually a valid assumption since TPA is the strongest among multi-photon absorption transitions. This dependence was found describing well fs-laser polymerisation/printing [25].

Figure 7(a) shows the transmittance $T = 10^{-OD} \equiv e^{-\alpha d}$ data measured on free-standing Si wafer. From the recognisable interference fringes at longer side of the spectrum, the Fabry-Pérot etalon fringes are recognisable and corresponds to the thickness of Si slab $d = 12$ μm (considering $n = 3.59$ at around $\lambda = 1$ μm). The slab transmittance $T = \frac{(n-1)^2}{n^2+1} \approx 48.3\%$ and reflectance $R = \frac{2n}{n^2+1} \approx 51.7\%$ at normal incidence at the spectral region with weak absorption with $n = 3.59$. Such values closely matched the experimental observation at the wavelengths close to the bandgap $E_g = 1.12$ eV or λ_g [μm] = $1.24/(E_g$ [eV])= 1.11 μm. This implies that the absorption is negligible with $\kappa \to 0$; the absorption coefficient $\alpha = 4\pi\kappa/\lambda$. Strong absorption is defined as $\alpha d > 1$ and for $d = 10$ μm $\alpha > 10^3$ cm^{-1}.

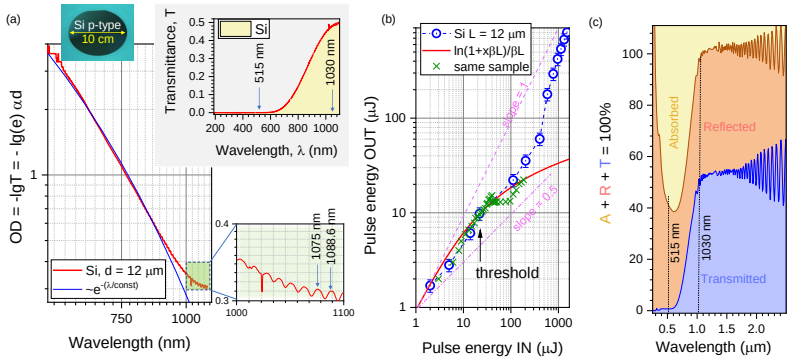

Figure 7. Transmission of micro-thin Si wafer. (a) Transmittance though $d \approx 12$ μm thick Si wafer; note log-log presentation for absorbance OD vs. λ. Thickness is determined from interference fringes: $\lambda_{1,2}$ are two adjacent maxima: $d = 1/[2(1/\lambda_1 - 1/\lambda_2)n]$ with $n = 3.59$ at 1080 nm wavelength. (b) Transmittance at $\lambda = 1030$ nm through the $L = 12$ μm thick Si wafer. Each irradiation point was refreshed using pre-programmed sample scan during measurement. Focusing was with $NA = 0.14$ objective lens into focal spot of radius $r = 0.61\lambda/NA \approx 4.49$ μm and the depth of focus $2z_R = \pi r^2/\lambda > d$. Single pulse ablation threshold was recognisable (under microscope) at $E_p^{IN} = 22$ μJ. Fit by $\ln(1 + x\beta L)/(\beta L)$ is shown with two photon absorption coefficient $\beta = 858$ cm/TW; x is the input pulse energy (intensity). The error bars are 15%. Cross markers shows data for the same sample and focusing conditions only for smaller step in energy between adjacent irradiation spots. (c) Portions (color-coded) of the absorbed A, reflected R and transmitted T power through the 12 μm-thick Si slab measured using an integrating sphere (Lambda 1050 UV/VIS/NIR spectrometer; PerkinElmer).

The power dependence of transmittance was measured to explore departure from the linear law, i.e., slope $\gamma = 1$ between transmitted pulse energy E_p^{OUT} vs. E_p^{IN} at the transparency wavelength of $\lambda = 1030$ nm (Fig. 7(b)). When the only nonlinear losses in transmission are due to two photon absorption (TPA), the first nonlinear absorption process, the transmitted power can be approximated by $I_{OUT} = I_{IN} \ln(1 + I_{IN}\beta L)/(\beta L)$, where L is the interaction length and β is the TPA coefficient. This model was used to describe an energy deposition by ultra-short laser pulse into polymerisable resin [25]. In

Preprints (www.preprints.org) | NOT PEER-REVIEWED | Posted: 30 December 2022 doi:10.20944/preprints202212.0583.v1

our case, the depth of focus or double Rayleigh length $2z_R = \pi r^2/\lambda = 61.5$ μm was larger than the sample and $L = 12$ μm was used; radius of focal spot $r = 0.61\lambda/NA = 4.5$ μm. Transmitted power (pulse energy) was measured during 10 s scan with refreshing irradiation spot by $\Delta X = 100$ μm, which is larger that the focal diameter of ~ 9 μm. A clear departure from the linear transmittance $\gamma = 1$ was observed and TPA coefficient $\beta = 858$ cm/TW. Interestingly, at higher pulse energies, reverse trend was observed showing larger T returning to the linear $\gamma = 1$ slope. Since measurements were carried out for single pulses and refreshed surface area for each laser shot, this transmittance increase reflects the induced transparency at high irradiance. The single pulse ablation threshold was observed at $E_p^{IN} = 22$ μJ, which corresponds to average fluence $F_p = 34.8$ J/cm^2/pulse and $I_p = F_p/t_p = 151$ TW/cm^2/pulse for pulse duration $t_p = 230$ fs. This is more that two orders of magnitude larger than for the thick (≥ 100 μm) Si (0.2 J/cm^2/pulse [24]). This is understandable due to lack of absorbance A since reflectance R and transmittance T makes $R + T \approx 1$ with negligible portion of A at wavelength of irradiation $\lambda = 1030$ nm (Fig. 7).

Figure 7(c) shows portions of experimentally measured reflected and transmitted light power at different wavelengths. Only a few-% of light is absorbed at $\lambda = 1030$ nm and a high portion of light $\sim 50\%$ reflects over the transparency window in the near-IR due to the high real part of the refractive index of Si $n \approx 3.6$. The low absorbance caused the higher pulse energy required for laser ablation of transparent Al_2O_3 mask patterning. It is also a fundamental cause of poor light harvesting by thin solar cells. When a thicker 50 nm Al_2O_3 mask was used on Si, the reflectivity was reduced due to smaller refractive index contrast. However, a larger pulse energy is required for ablating a hole through a thicker transparent mask film. As a result, a deeper energy deposition takes place and cause formation of high aspect ratio structures after plasma etching (Fig. 5).

3.5. Minority carriers lifetime

One of the industry accepted quality tests for solar cell performance is measurement of the minority carrier lifetime. A short lifetime and high surface recombination velocity S limits collection of photo-carriers outside the solar cell, hence, reduce the efficiency of light-to-electricity power conversion. We used the Sinton WCT-100 instrument which works via inductive detection of the total recombination currents in the bulk and on the surface. A light flash creates photo-excited carriers, electrons-hole pairs e-h with concentration $\Delta n = \Delta p$, which are much smaller than that due to doping (n or p). That is orders of magnitude higher in solar cells $p \approx 10^{17} - 10^{18}$ cm^{-3} used for high efficiency including those with the IBC architecture. The diffusion coefficient of the minority carriers D_{mc} [cm^2/s] defines the surface recombination lifetime $\tau_s = \frac{4}{D_{mc}}\left(\frac{W}{\pi}\right)^2$ for one recombination active surface with high surface recombination velocity S [cm/s] (other is perfectly passivated $S = 0$) and W is the thickness of the cell. A general expression is $\tau_s = \frac{W}{2S} + \frac{1}{D_{mc}}\left(\frac{W}{\pi}\right)^2$ for both solar cell surfaces having the same $S = S_1 = S_2$ on both surfaces. The effective carrier lifetime is defined by the bulk and surface contributions $1/\tau_{eff} = 1/\tau_b + 1/\tau_s$. For the quasi-steady-state (QSS) $\tau_{eff} \gg \frac{W^2}{\pi^2 D_{mc}}$. For low doping concentrations $N_D \leq 7 \times 10^{17}$ cm^{-3} $S \approx 70$ cm/s [26]; the "geometrical" contribution to τ_s, namely, $\frac{W}{2S} = 5$ μs for $W = 10$ μm thickness Si cell and $S = 10^2$ cm/s. This estimate shows that Si solar cells of tens-of-micrometre thickness need good passivation to reduce surface losses of photo-generated carriers. The S is defined $S = N_{ss} v_{th} \sigma$ by the surface state density N_{ss} [cm^{-2}] of recombination centers at the surface, the average thermal velocity $v_{th} = \sqrt{3k_B T/m^*} \approx 10^7$ cm/s ($T = 300$ K) and the σ [cm^2] is the recombination cross-section of the recombination center (k_B is the Boltzmann constant, m^* is the effective mass of the charge carrier, T is the absolute temperature).

Figure 8 summarises the lifetime measurements from equivalent area samples treated by different processing steps used in PhC texturing of Si for solar cell applications, e.g., Cr coating, Cr wet etch removal, Cr mask ablation, KOH and RIE patterned Si surfaces of the final design after Cr-mask removal. The lifetime of as-received Si wafer was $\tau_{mc} \sim 12$ μs,

Preprints (www.preprints.org) | NOT PEER-REVIEWED | Posted: 30 December 2022 doi:10.20944/preprints202212.0583.v1

which is typical for the Czochralski grown material 10-50 μs and is 50-150 μs for the float-zone Si [27]. It was revealed that e-beam evaporation of Cr mask and its subsequent removal already significantly reduced τ_{mc}. Direct laser ablation of Si (without mask) showed only reduced the lifetime by half. Final PhC patterns after wet KOH or dry plasma etch had τ_{mc} typically reduced to 2 μs. These low values are caused by a significant contribution of the surface recombination. Surface recombination rate can be reduced by thermal treatments up to 450°C, by passivisation and anti-reflection coatings applied for the actual Si solar cells. Here we compared the evolution of τ_{mc} under processing steps required for PhC definition using different mask application, fabrication and removal steps. It was encouraging to find that the laser ablation itself was not the main contributor to reduced the carrier lifetime values. This was expected since the Si volume removed by etch (wet or dry) was from the region directly irradiated by laser during mask ablation. The volume most affected by the laser is removed during the formation of the PhC surface texture for light trapping. Interestingly, τ_{mc} measured from the Si surface just after ablation of holes (without Cr mask as in the inset of Figure 6(a)), showed slightly larger τ_{mc} values after one week at room conditions, most probably, due to passivisation by oxidation. All the τ_{mc} measurements were carried out on the same sized samples. In a separate experiment we have established that τ_{mc} can significantly vary up to a factor of 2-3 just because of the sample size (respective to the size of inductive coil-reader in the center of the measuring pad).

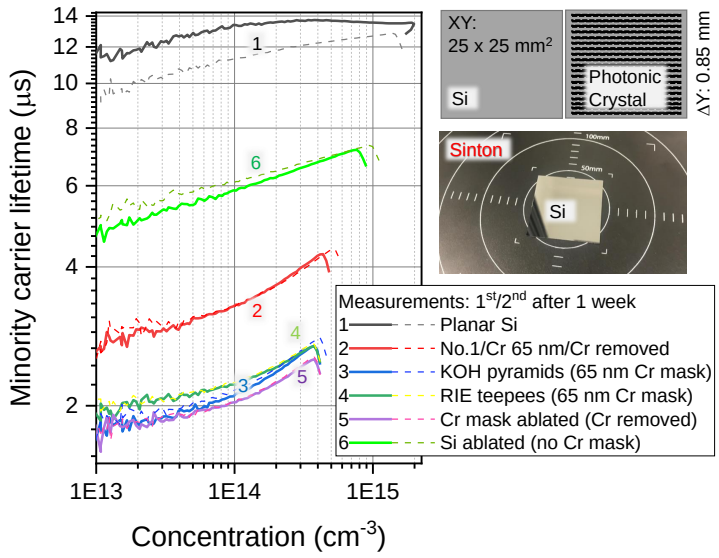

Figure 8. The lifetime of minority carriers τ_{mc} vs concentration in Si with different surface treatments measured with Sinton (Si p-type, Boron-doping). Inset shows schematics of the fabricated patterns on 25×25 mm^2 area samples. Photonic crystal structures with $\Lambda = 3.1$ μm period were laser patterned with $\Delta y = 0.85$ mm separation ($\sim$ 15% coverage of the surface by PhC was made). The quasi-steady-state (QSS) mode of calculations was carried out with optical factors $f = 0.7$ (not-textured No. 1,2) and $f = 0.95$ (textured No. 3,4,5,6) samples. Si-wafer here was 300 μm thick, Cr film used for mask was e-beam deposited.

4. Conclusions and Outlook

The light trapping at the near-bandgap wavelengths of Si $\sim$ 1 μm can be enhanced using PhC textured Si surfaces. Fabrication of such PhC patterns using dielectric transparent Al_2O_3 mask was made at different thicknesses, 20 and 50 nm. Such masks are promising due to better surface quality and avoidance of metallic mask, e.g., Cr, which causes reduced lifetime of minority carriers leading reduced efficiency of the eventual Si solar cell. Also, direct patterning of Si surface by ablation (even without a dielectric mask) can be made for

 doi:10.20944/preprints202212.0583.v1

plasma etching of PhC patterns. It was found that thicker Al_2O_3 mask caused fabrication of higher aspect ratio structures (deeper holes). This is caused by reduced reflectivity of surface due to Al_2O_3 coating and larger pulse energy required to open a hole in the mask. The holes in Al_2O_3 mask have not shown melting signatures as compared with Cr-mask used earlier [8]. The minority carriers lifetime tests showed strong dependence of τ_{mc} values on surface treatments which are required for PhC patterning of light trapping surface.

Analysis of $12-\mu$m-thick Si transmission and energy deposition during fs-laser patterning revealed presence of an optical nonlinearity (departure from the linear transmittance at $slope = 1$), which was directly measured due to virtue of small thickness. An upper bound of TPA for Si at $\lambda = 1030$ nm was estimated as $\beta = 858$ cm/TW. This high effective value is affected by thickness of Si, where reflections from both surfaces contribute to T and R (hence also $A \equiv 1 - R - T$).

Author Contributions: Conceptualization, Saulius Juodkazis; Methodology, Haoran Mu; Validation, Haoran Mu, Tomas Katkus, Mantas Vaičiulis and Soon Hock Ng; Formal analysis, Jovan Maksimovic, Haoran Mu, Daniel Smith, Mantas Vaičiulis, Ramūnas Aleksiejūnas, Gediminas Seniutinas and Saulius Juodkazis; Investigation, Jovan Maksimovic, Haoran Mu, Daniel Smith and Tomas Katkus; Resources, Tomas Katkus, Mantas Vaičiulis and Ramūnas Aleksiejūnas; Writing – original draft, Jovan Maksimovic and Saulius Juodkazis; Writing – review and editing, Jovan Maksimovic, Haoran Mu, Daniel Smith, Tomas Katkus, Ramūnas Aleksiejūnas, Gediminas Seniutinas, Soon Hock Ng and Saulius Juodkazis; Visualization, Jovan Maksimovic, Haoran Mu and Saulius Juodkazis; Supervision, Soon Hock Ng and Saulius Juodkazis; Funding acquisition, Soon Hock Ng and Saulius Juodkazis.

Funding: Please add: "This research received no external funding" or "This research was funded by NAME OF FUNDER grant number XXX." and and "The APC was funded by XXX". Check carefully that the details given are accurate and use the standard spelling of funding agency names at https://search.crossref.org/funding, any errors may affect your future funding.

Data Availability Statement: In this section, please provide details regarding where data supporting reported results can be found, including links to publicly archived datasets analyzed or generated during the study. Please refer to suggested Data Availability Statements in section "MDPI Research Data Policies" at https://www.mdpi.com/ethics. If the study did not report any data, you might add "Not applicable" here.

Acknowledgments: We are grateful to Workshop of Photonics Ltd., Lithuania for fs-laser fabrication setup acquired via a technology transfer project in 2012. We are grateful for the financial support via ARC Linkage LP190100505 and the ARC Discovery DP190103284 projects. Discussions of solar cells applications with Prof. Sajeev John and Prof. Robby Peibst are acknowledged.

Conflicts of Interest: Declare conflicts of interest or state "The authors declare no conflict of interest." Authors must identify and declare any personal circumstances or interest that may be perceived as inappropriately influencing the representation or interpretation of reported research results. Any role of the funders in the design of the study; in the collection, analyses or interpretation of data; in the writing of the manuscript, or in the decision to publish the results must be declared in this section. If there is no role, please state "The funders had no role in the design of the study; in the collection, analyses, or interpretation of data; in the writing of the manuscript, or in the decision to publish the results".

Appendix A. Reflection color

Color change of a Al_2O_3 mask after plasma etching was indicating a change of thickness h. The reflection coefficient for E-field for a thin film on a highly reflective substrate is given by [28]:

$$r = \frac{r_{12} + r_{23}e^{2i\beta}}{1 + r_{12}r_{23}e^{2i\beta}}, \tag{A1}$$

where $\beta = \frac{2\pi}{\lambda} n_2^* h \cos\theta_2$, θ_2 is refraction angle and r_{ij} is the polarisation dependent Fresnel reflection coefficient for the angle of incidence θ_1 (integers $i, j = 1 \ldots 3$ marks ambient 1 (air), 2(Al_2O_3) and 3 (Si)). Figure S1(a) shows the different contributions to reflectance,

Preprints (www.preprints.org) | NOT PEER-REVIEWED | Posted: 30 December 2022 doi:10.20944/preprints202212.0583.v1

which cause color appearance of the film, e.g., Al_2O_3-mask. Reflectance R (Fig. S1(b)) of such film is mapped onto (x, y) color coordinates on the chromaticity map (380-780 nm visible colors).

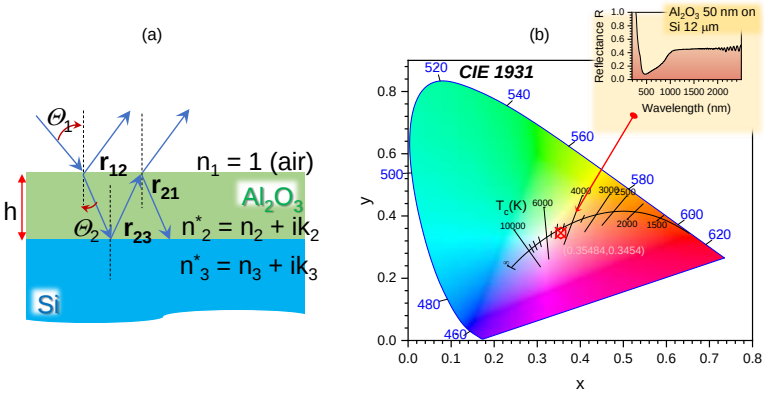

Figure S1. (a) Schematics and conventions for reflection coefficient r (Eqn. A1) from a thin film (Al_2O_3) of thickness h on Si; reflectance $R \equiv |r|^2$ and n_i^* is the complex refractive coefficient of the i^{th}-layer. (b) Chromaticity plot for reflectance R from a 50-nm-Al_2O_3 coated 12-μm-Si film (inset shows spectrum $R(\lambda)$). The marker points to the $(x, y) = (0.35484, 0.3454)$ point.

Alumina has amphoteric nature and can be desolved in basic KOH wet etch as well as acidic, e.g. HF based solutions. Color change provides sensitive feedback for mask changes in dry (Fig. 5) and wet etching.

Appendix B. Focal spot size: definitions

It is convenient to define the focal spot size by the Airy disk, i.e., the first minimum of the focused plane wave as $1.22\lambda/NA = 2.44\lambda f_\#$, where f-number $f_\# \equiv F/D$ and numerical aperture $NA = n\sin\left[\arctan\left(\frac{1}{2f_\#}\right)\right] \approx n\frac{1}{2f_\#}$, which is valid as long as $\sin\alpha \approx \tan\alpha$ or $f_\# > 1.2$ (fast focusing is at smaller $f_\#$); D is the diameter of beam/aperture, F is the focal length and n refractive index at focus. The Airy disk contains 86% of the laser pulse/beam energy. It comparable with a transmitted power of the Gaussian pulse/beam through the aperture which has radius of the beam waist $1 - e^{-2} = 86.5\%$. When laser beam is expanded and only central part is entering the objective lens (clipped on the entrance pupil aperture), the intensity at the focus resembles Airy pattern with a ring, however, when diameter of a Gaussian pulse/beam is closely matching the entrance pupil, the intensity at the focus is Gaussian-like with radial profile $I(r) = I_0 e^{-2r^2/w_0^2}$, where w_0 is the waist (radius).

For the Gaussian beam focused with a lens of $f_\# = F/D = 1/(2NA)$ the focal spot is $2w_0 = \frac{4\lambda}{\pi} \times \frac{F}{D} = \frac{4\lambda}{\pi} f_\# = \frac{4\lambda}{\pi} \times \frac{1}{2NA}$ (in air) and the depth-of-focus where beam is expanding by $\sqrt{2}$ factor is $DoF = \frac{8\lambda}{\pi} \times \left(\frac{F}{D}\right)^2$. For example, with $NA = 0.7$ and $\lambda = 515$ nm waist $w_0 = 234$ nm (Gaussian) or $r_f = 0.61\lambda/NA = 449$ nm (Airy disk). The Gaussian beam intensity is stronger localised than the central Airy disk. For the tight (fast) focusing when validity of $\sin\alpha = \tan\alpha$ breaks, e.g., at $NA = 0.9$, a direct estimate of the beam waist could be obtained from the slope of the linear fit of the ablation pit diameter on pulse energy $D_a^2 = f(\ln(E_p))$:

$$D_a^2 = 2w_0^2\left(\ln(E_p) + \ln\left[\frac{2}{\pi w_0^2 F_{th}}\right]\right), \tag{A2}$$

where $F_p = E_p/(\pi w_0^2)$ is the fluence (F_{th} is the threshold fluence when $D \to 0$).

This approach also accounts for the beam quality factor M^2 which is 1 for the ideal Gaussian pulse but can have range of values 1.1 - 1.5 for the actual laser beam/pulse. This experimental dependence also defines the threshold ablation value at the cut off value of $D \to 0$. For the Gaussian pulse/beam, the average intensity $I_p = E_p/(\pi w_0^2 t_p)$ is half

of the peak intensity $I_0 = 2I_p$. The full angular width of diverging angle after the focus is $\theta_d = D/F = 1/f_\#$ for the Gaussian beam. The full width half maximum (FWHM) of the Gaussian intensity profile is related to the waist $FWHM = \sqrt{2\ln 2}w_0 \approx 1.18w_0$. The intensity of $0.5I_p$ is at $0.59w_0$, I_p/e at $0.71w_0$ and I_p/e^2 (13.5% level) at w_0.

References

1. Wilson, G.M.; Al-Jassim, M.; Metzger, W.K.; Glunz, S.W.; Verlinden, P.; Xiong, G.; Mansfield, L.M.; Stanbery, B.J.; Zhu, K.; Yan, Y.; et al. The 2020 photovoltaic technologies roadmap. *Journal of Physics D: Applied Physics* **2020**, *53*, 493001. doi:10.1088/1361-6463/ab9c6a.
2. Green, M.A.; Dunlop, E.D.; Hohl-Ebinger, J.; Yoshita, M.; Kopidakis, N.; Hao, X. Solar cell efficiency tables (version 59). *Progress in Photovoltaics: Research and Applications* **2022**, *30*, 3–12. doi:10.1002/pip.3506.
3. Jager-Waldau, A. Progress in chalcopyrite compound semiconductor research for photovoltaic applications and transfer of results into actual solar cell production. *Solar Energy Materials and Solar Cells* **2011**, *95*, 1509–1517. Special Issue : Thin film and nanostructured solar cells.
4. Wolden, C.; K., J.; Baxter, J.; Repins, I.; Shaheen, S.; Torvik, J.; Rockett, A.; Fthenakis, V.; Aydil, E. Photovoltaic manufacturing: Present status, future prospects, and research needs. *Journal of Vacuum Science and Technology A* **2011**, *29*.
5. Arnulf, J.W. Photovoltaic Status Report 2019. *Publications Office of the EU* **2019**, *1*.
6. Boriskina, S.V.; Green, M.A.; Catchpole, K.; Yablonovitch, E.; Beard, M.C.; Okada, Y.; Lany, S.; Gershon, T.; Zakutayev, A.; Tahersima, M.H.; et al. Roadmap on optical energy conversion. *J Optics* **2016**, *18*, 073004.
7. Ludin, N.A.; Mustafa, N.I.; Hanafiah, M.M.; Ibrahim, M.A.; Asri Mat Teridi, M.; Sepeai, S.; Zaharim, A.; Sopian, K. Prospects of life cycle assessment of renewable energy from solar photovoltaic technologies: A review. *Renewable and Sustainable Energy Reviews* **2018**, *96*, 11–28. doi:10.1016/j.rser.2018.07.048.
8. Maksimovic, J.; Hu, J.; Ng, S.H.; Katkus, T.; Seniutinas, G.; Pinedo Rivera, T.; Stuiber, M.; Nishijima, Y.; John, S.; Juodkazis, S. Beyond Lambertian light trapping for large-area silicon solar cells: fabrication methods. *Opto-Electronic Advances* **2022**, *5*, 210086.
9. Bhattacharya, S.; Baydoun, I.; Lin, M.; John, S. Towards 30% Power Conversion Efficiency in Thin-Silicon Photonic-Crystal Solar Cells. *Phys. Rev. Applied* **2019**, *11*, 014005.
10. Eyderman, S.; John, S. trapping and Recycling for Extraordinary Power Conversoin in Ultra-thin Gallium-Arsenide Solar Cells. *Scientific Reports* **2016**, *6*, 28303.
11. Eyderman, S.; John, S.; Deinega, A. Solar light trapping in slanted conical-pore photonic crystals: Beyond statistical ray trapping. *J. Appl. Phys.* **2013**, *113*, 154315.
12. A.Deinega.; S.Eyderman.; S.John. Coupled optical and electrical modeling of solar cell based on conical pore silicon photonic crystals. *J. Appl. Phys.* **2013**, *113*, 224501.
13. Chutinan, A.; John, S. Light trapping and absorption optimization in certain thin-film photonic crystal architectures. *Phys. Rev. A* **2008**, *78*, 023825.
14. Mavrokefalos, A.; Han, S.E.; Yerci, S.; Branham, M.S.; Chen, G. Efficient Light Trapping in Inverted Nanopyramid Thin Crystalline Silicon Membranes for Solar Cell Applications. *Nano Lett.* **2012**, *12*, 2792 – 2796.
15. Foster, S.; John, S. Light-trapping design for thin-film silicon-perovskite tandem solar cells. *J. Appl. Phys.* **2016**, *120*, 103103.
16. Kuang, P.; Eyderman, S.; Hsieh, M.L.; Post, A.; John, S.; Lin, S.Y. Achieving an Accurate Surface Profile of a Photonic Crystal for Near-Unity Solar Absorption in a Super Thin-Film Architecture. *ACS Nano* **2016**, *10*, 6116–6124.
17. Shockley, W.; Queisser, H.J. Detailed Balance Limit of Efficiency of p-n Junction Solar Cells. *Journal of Applied Physics* **1961**, *32*, 510–519. doi:10.1063/1.1736034.
18. Kaneka achieves new efficiency record for a practical size crystalline silicon PV cell. PV magazine: https://www.pv-magazine.com/2016/09/19/, 2016.
19. Haase, F.; Hollemann, C.; Schäfer, S.; Merkle, A.; Rienäcker, M.; Krügener, J.; Brendel, R.; Peibst, R. Laser contact openings for local poly-Si-metal contacts enabling 26.1%-efficient POLO-IBC solar cells. *Solar Energy Materials and Solar Cells* **2018**, *186*, 184–193. doi:https://doi.org/10.1016/j.solmat.2018.06.020.
20. Hollemann, C.; Haase, F.; Schäfer, S.; Krügener, J.; Brendel, R.; Peibst, R. 26.1%-efficient POLO-IBC cells: Quantification of electrical and optical loss mechanisms. *Prog. Photovoltaics* **2019**, *27*, 950–958.
21. Han, M.; Smith, D.; Ng, S.H.; Vilagosh, Z.; Anand, V.; Katkus, T.; Reklaitis, I.; Mu, H.; Ryu, M.; Morikawa, J.; et al. THz Filters Made by Laser Ablation of Stainless Steel and Kapton Film. *Micromachines* **2022**, *13*, 1170.
22. Juodkazis, S.; Nishi, Y.; Misawa, H.; Mizeikis, V.; Schecker, O.; Waitz, R.; Leiderer, P.; Scheer, E. Optical transmission and laser structuring of silicon membranes. *Opt. Express* **2009**, *17*, 15308–15317.
23. Liu, X.Q.; Yu, L.; Yang, S.N.; Chen, Q.D.; Wang, L.; Juodkazis, S.; Sun, H.B. Optical Nanofabrication of Concave Microlens Arrays. *Laser Photonics Reviews* **2019**, *13*, 1800272.
24. Bonse, J.; Baudach, S.; Krüger, J.; Kautek, W.; Lenzner, M. Femtosecond laser ablation of silicon–modification thresholds and morphology. *Applied Physics A* **2002**, *74*, 19–25.
25. Miwa, M.; Juodkazis, S.; Kawakami, T.; Matsuo, S.; Misawa, H. Femtosecond Two-photon Stereo-lithography. *Appl. Phys. A* **2001**, *73*, 561–566.

26. Markvart, T.; Castañer, L. Chapter I-1-A - Principles of Solar Cell Operation. In *McEvoy's Handbook of Photovoltaics (Third Edition)*, Third Edition ed.; Kalogirou, S.A., Ed.; Academic Press, 2018; pp. 3–28. doi:https://doi.org/10.1016/B978-0-12-809921-6.00001-X.
27. Thomas, R. 24 - SILICON SOLAR CELLS (1) — BASICS. In *Solar Energy Conversion*; Dixon, A.; Leslie, J., Eds.; Pergamon, 1979; pp. 785–803. doi:https://doi.org/10.1016/B978-0-08-024744-1.50029-2.
28. Thick Slabs and Thin Films. In *The Physics of Thin Film Optical Spectra: An Introduction*; Springer Berlin Heidelberg: Berlin, Heidelberg, 2005; pp. 101–124. doi:10.1007/3-540-27905-9_7.